Organic-inorganic hybrid ZIF-8/MXene/cellulose-based textiles with improved antibacterial and electromagnetic interference shielding performance

Zhaochuan Yu [a,b], Chao Deng [a,c,d,*], Chenhui Ding [c], Xing Zhang [e], Yuqian Liu [a], Chao Liu [a], Zhichao Lou [a], Farzad Seidi [a], Jingquan Han [a], Qiang Yong [a], Huining Xiao [b,**]

[a] International Innovation Center fo Forest Chemicals and Materials and Jiangsu Co-Innovation Center for Efficient Processing and Utilization of Forest Resources, Nanjing Forestry University, Nanjing 210037, China
[b] Department of Chemical Engineering, University of New Brunswick, Fredericton, NB E3B 5A3, Canada
[c] Macromolecular Chemistry and Bavarian Polymer Institute, University of Bayreuth, 95440 Bayreuth, Germany
[d] Key Laboratory of Clean Dyeing and Finishing Technology of Zhejiang Province, Shaoxing University, Shaoxing 312000, China
[e] College of Textile and Fashion, Hunan Institute of Engineering, Xiangtan, Hunan 411104, China

A R T I C L E   I N F O

A B S T R A C T

Despite the tremendous efforts on developing antibacterial wearable textile materials containing $Ti_3C_2T_x$ MXene, the singular antimicrobial mechanism, poor antibacterial durability, and oxidation susceptibility of MXene limits their applications. In this context, flexible multifunctional cellulosic textiles were prepared via layer-by-layer assembly of MXene and the in-situ synthesis of zeolitic imidazolate framework-8 (ZIF-8). Specifically, the introduction of highly conductive MXene enhanced the interface interactions between the ZIF-8 layer and cellulose fibers, endowing the green-based materials with outstanding synergistic photothermal/photodynamic therapy (PTT/PDT) activity and adjustable electromagnetic interference (EMI) shielding performance. In-situ polymerization formed a MXene/ZIF-8 bilayer structure, promoting the generation of reactive oxygen species (ROS) while protecting MXene from oxidation. The as-prepared smart textile exhibited excellent bactericidal efficacy of >99.99 % against both *Escherichia coli* (*E. coli*) and *Staphylococcus aureus* (*S. aureus*) after 5 min of NIR (300 mW cm^{-2}) irradiation which is below the maximum permissible exposure (MPE) limit. The sustained released Zn^{2+} from the ZIF-8 layer achieved a bactericidal efficiency of over 99.99 % within 48 h without NIR light. Furthermore, this smart textile also demonstrated remarkable EMI shielding efficiency (47.7 dB). Clearly, this study provides an elaborate strategy for designing and constructing multifunctional cellulose-based materials for a variety of applications.

1. Introduction

In recent years, with the increasing popularity of smart wearable electronic devices, smart textiles that are lightweight, flexible, comfortable, and convenient have attracted enormous research interests [1–4]. Numerous materials possessing exceptional properties are incorporated into textiles to execute diverse functionalities, including energy harvesting and storage, electromagnetic interference (EMI) shielding, bio-protection, sensing, and medical treatment [5–7]. Commercially available synthetic polymer-based (such as polyester fibers, nylon fibers, and acrylic fibers) or bio-based (such as plant cellulose fibers, wool, and silk) textiles are considered as suitable substrates for manufacturing smart textiles due to their inherent flexibility, comfortability, and processability. Particularly, cellulose fibers have become a research hotspot due to their renewable, biodegradable, and environmentally friendly characteristics. Generally, the developed smart textiles are inevitably in direct or indirect contact with human body in the process of use. Certain highly pathogenic bacteria and viruses could persist on the surface of textiles for an extended period of time, ranging from a few days to several weeks, and these pathogenic bacteria could

cause cross-contamination and pose a significant threat to the health of individuals [8,9]. To solve this problem, researchers attempted to introduce bactericides into textiles, and successfully developed various bioprotective textiles with antibacterial and antiviral capabilities [10,11]. However, the extensive use of traditional bactericides posed the risk of drug resistance. Furthermore, wearable textile materials having outstanding electromagnetic interference shielding performance are also crucial for effectively addressing the growing threat of electromagnetic radiation pollution [12]. Therefore, the development of smart textiles that combine innovative sterilization strategies and EMI shielding performance is essential to effectively address the complex challenges of bio-protection in diverse environments.

At present, novel antibacterial and antiviral strategies based on diverse physical or chemical sterilization methods have been extensively investigated, including mechanical damage to cell membranes, release of bactericidal metal ions, electromagnetic wave and electron beam sterilization, photothermal therapy (PTT), and photodynamic therapy (PDT) [13–19]. Among the above-mentioned numerous bactericidal strategies, synergistic PTT/PDT steadily emerged as a prominent area of research due to its numerous advantages, including controllable and significant bactericidal effect without any risk of drug resistance [20,21]. Specifically, 2D flexible nano-photosensitizer MXene ($Ti_3C_2T_x$) materials attracted great interest recently due to its localized surface plasmon resonance (LSPR) effect, better biocompatibility, hydrophilicity, high specific surface area and abundant surface functional groups (—F, =O, and -OH) [12,22,23]. These characteristics enable it to effectively enhance the functionality of various textile materials. Furthermore, MXene also exhibits high electrical conductivity and dielectric loss, making it one of the top materials of choice for enhancing EMI shielding performance [24,25]. Tang et al. prepared a MXene-functionalized nanocellulose membrane using a layer-by-layer self-assembly method, which can achieve rapid sterilization under near-infrared laser irradiation (808 nm, 1000–2000 mW cm^{-2}) [26]. Yan et al. successfully deposited active MXene nanosheets in situ onto silk fibers through a dip-coating method, creating a multifunctional textile with rapid PTT antibacterial and UV resistance capabilities [27]. Although PTT/PDT materials based on MXene have been developed, challenges still remain in the MXene PDT process due to inadequate oxygen supply and the rapid recombination rate of photogenerated carriers, hindering the generation of reactive oxygen species (ROS) during energy transfer [28]. It was reported that PDT operates through two mechanisms: type I pathway involves the generation of superoxide radicals ($\cdot O^{2-}$) and hydroxyl radicals ($\cdot OH$) via electron transfer or hydrogen atom abstraction, while type II pathway PDT generates singlet oxygen ($^1O_2$) by energy transfer. The type II PDT pathway is present in most PDT photosensitizers and heavily relies on the O_2 level in the tissue environment, whereas the type I pathway is less dependent on oxygen [29]. Improving the oxygen supply environment for the MXene PDT process, promoting charge transfer to stabilize the excited state, and reducing the energy required for the excited state are crucial for the development of MXene-based synergistic PTT/PDT antibacterial materials [30,31]. It is worth mentioning that for most of the developed MXene PTT/PDT strategies to function completely, it is required that the light intensity of NIR laser (808 nm) irradiation is over 1000 mW cm^{-2}, which is above the maximum permissible exposure (MPE) (330 mW cm^{-2}, 808 nm) to skin and tissue [26,29,32,33]. Additionally, the spontaneous oxidation of the MXene surface in the presence of water and oxygen could also be a matter of concern, as it may lead to a degradation in the performance of MXene [34]. Therefore, it is necessary to develop a novel MXene modification strategy to further overcome these limitations.

Materials with metal-organic frameworks (MOF) are nanocarriers composed of metal ion clusters and organic ligands. MOF materials possess unique topological structures consisting of regularly shaped pores and channels, allowing for the separation or blocking of specific molecules [35]. Furthermore, the unique combination of central metal ions and organic ligand frameworks in MOFs provides the potential for facilitating intermolecular charge transfer [36]. Among the various MOF materials, the imidazole acid molecular sieve framework-8 (ZIF-8) stands out as a unique antimicrobial MOF material [37–39]. Its topological structure resembles zeolites with pore size approximately 3.4 Å, effectively preventing the contact of water molecules and serving as an oxygen storage medium in photocatalysis [40,41]. Moreover, the slow release of Zn^{2+} from ZIF-8 could provide a durable antibacterial effect [42]. Choi et al. improved the stability of Ti-MXene films by covering them with continuous layers of ZIF-8 [34]. Zhang et al. constructed a (ZIF-8)-enhanced PTT/PDT antibacterial platform by electrospinning MXene/ZIF-8 dispersed in polylactic acid solution, which could promote wound healing [28]. Therefore, ZIF-8 has the potential to enhance MXene PTT/PDT activity and provide an antioxidative barrier for the wearable materials bearing MXene.

Prior to developing a series of advanced smart textiles, two challenges must be addressed: 1) an appropriate strategy to assemble MXene/ZIF-8 functional layers on the surface of cellulose fibers or nonwoven fibric while preventing the oxidation of MXene; 2) achieving rapid and long-lasting antibacterial effects through multiple antibacterial mechanisms. To address these issues specifically, in this work, we developed a novel strategy for the fabrication of organic-inorganic hybrid materials through interface assembly and in-situ growth processes, resulting in cellulosic wearable smart textiles with synergistic PTT/PDT antibacterial and EMI shielding properties. Initially, a robust and stable NIR light-responsive PTT/PDT MXene ($Ti_3C_2T_x$) layer was established on the surface of cellulose nonwovens (CNWs) through hydrogen bonding and electrostatic interactions. Subsequently, the ZIF-8 was in-situ grown on the MXene layer to enhance th0e PDT activity of the textiles and to provide a durable antibacterial effect (Scheme 1a). The prepared smart textiles exhibited excellent breathability and flexibility, and the assembled MXene/ZIF-8 bilayer structure could generate high heating and ROS based on the PTT/PDT effect. The smart textile achieved rapid killing of *E. coli* and *S. aureus* under NIR radiation (300 mW cm^{-2}, 808 nm) in 5 min, while NIR intensity remained below the MPE limit. The ZIF-8 layer not only gradually released Zn^{2+} to offer persistent antibacterial effects but also acts as a barrier against oxygen and water-induced oxidation of the MXene layer. Furthermore, this smart textile material surpasses previously reported textile-based shielding materials in terms of EMI shielding performance, leading to integrated wearable textiles with multi-functions suitable for a variety of applications (Scheme 1b).

2. Experimental section

2.1. Materials

Highly breathable and biodegradable cellulose-based nonwovens (CNWs) were produced by utilizing bleached softwood pulp and Lyocell fibers through wet-laid and hydroentanglement processes [11]. MAX (Ti_3AlC_2, NO: YY201702) powders were purchased from Jilin 11 technology Co., Ltd. $Zn(NO_3)_2.6H_2O$ (≥ 98 %) and hydrochloric acid solution (HCl, 36.5 %) were obtained from Nanjing Chemical Co., Ltd. Lithium fluoride (LiF, 99 %, NO: L434127) and 2-Methylimidazole (2-MIM, ≥ 99 %, NO: M104839) were purchased from Aladdin Biochemical Technology Co., Ltd. Luria-Bertani (LB, NO: HB0128) broth medium was purchased from Qingdao Hope Bio-Technology Co., Ltd. All the solvents used in the test were analytical grade and used without further purification.

2.2. Preparation of MXene ($Ti_3C_2T_x$) nanosheets suspension

The preparation of MXene ($Ti_3C_2T_x$) nanosheets was conducted by employing a mild hydrofluoric acid-like etching technique (Fig. 1a) reported in our previous work [11]. Initially, 40 mL of HCl (9 M) and 2 g of LiF were added to the Teflon reactor. Afterwards, 2 g of MAX (Ti_3AlC_2)
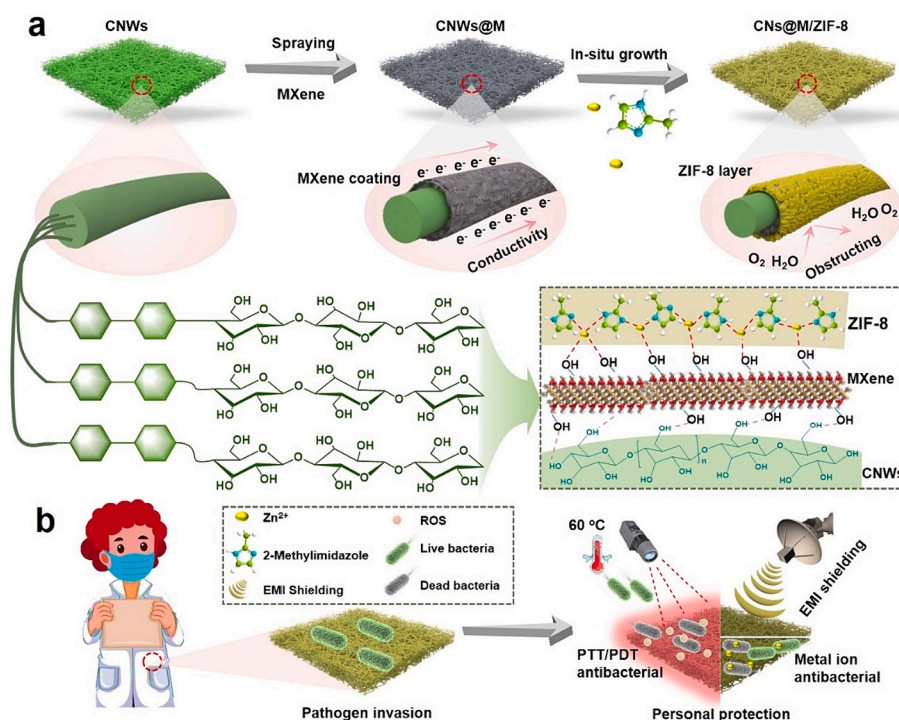
Scheme 1. Schematic illustrating the fabrication of functionalized CNWs@M/ZIF-8 and its applications. (a) Preparation process of CNWs@MXene/ZIF-8 (CNWs@M/ZIF-8) wearable materials on cellulosic nonwovens (CNWs). (b) Schematic of multi-protection of CNWs@M/ZIF-8, including highly bactericidal efficacy and outstanding EMI shielding.
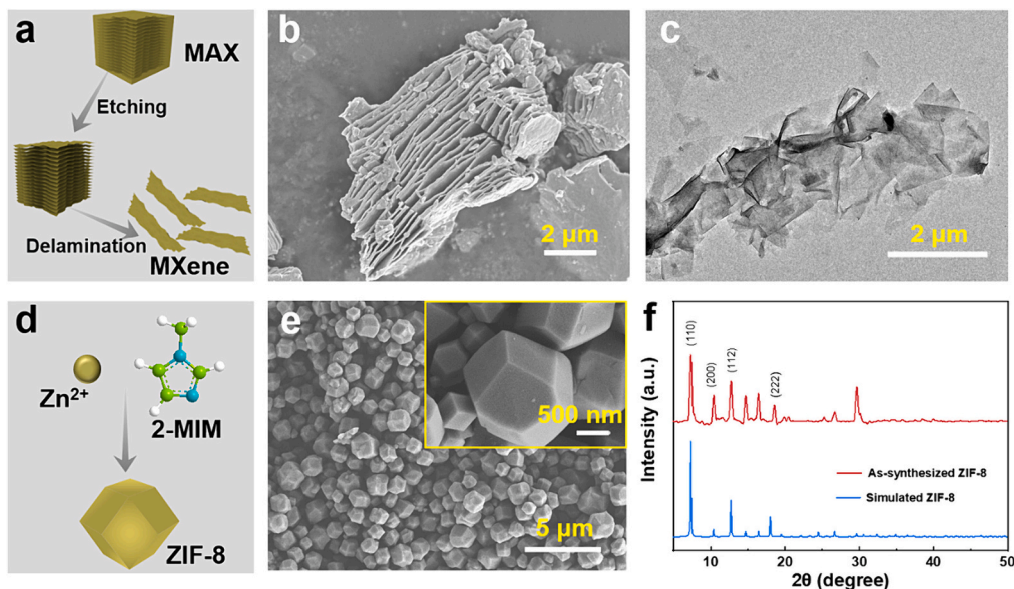
Fig. 1. Preparation and characterization of MXene and ZIF-8. (a) Schematic diagram for the fabrication of MXene. (b) SEM image of as-obtained layered MXene (Ti$_3$C$_2$) (9.4 mm × 8.0 K). (c) TEM image of MXene sheets (8.0 mm × 20.0 K). (d) Schematic diagram for the fabrication of ZIF-8. (e) SEM image of the crystalline structure formed by 2-MIM as an organic ligand and Zn^{2+}(ZIF-8) (8.9 mm × 5.0 K, 4 mm × 20.0 K). (f) XRD spectra of as-synthesized and simulated ZIF-8, wherein, the peaks located at 7.3°, 10.4°, 12.7°, and 18.5° respectively correspond to the (110) (200) (112) (222) crystal planes.

powder was slowly put into the reactor and left to stir at 35 °C for 24 h. To remove by-product hydrofluoric acid (HF) and other impurities, the resulting suspension was centrifuged for 10 min (1978 g, rcf) and then redispersed with deionized H$_2$O, which was repeated several times until the pH of the suspension reached around 6. The ethanol was added to the black sludge-like solid, sonicated for 60 min to obtain ethanol-intercalated multilayer nanosheets, and collected in tube after centrifugation at 16300 g (rcf) for 10 mins. Subsequently, deionized (DI) water was added into the pellet again, subjected to sonication at 750 W for 10 mins, followed by centrifugation at 1978 g (rcf) for a duration of 10 min, resulting in the production of MXene with a few layers. Furthermore, the gravimetric measurement of the concentration of MXene nanosheets was conducted following the freeze-drying of a certain quantity of the dispersion.

2.3. Fabrication of antibacterial textiles (CNWs@M/ZIF-8)

The CNWs (60×60 mm^2) were first soaked in ethanol (EtOH, 75 wt %)/NaOH (1 wt%) mixed aqueous solution for 1 h, and then dried at 50 °C to constant weight. Subsequently, the formulated MXene suspension was applied by spray coating onto CNWs and dried under vacuum at ambient temperature. To prepare CNWs with different MXene loadings (CNWs@M), the spraying and drying process was repeated several times [11]. Zn(NO$_3$)$_2$·6H$_2$O (12.1 g) and the organic ligand 2-MIM (106.7 g) were separately dissolved in 1.0 L of deionized water to obtain zinc ions (0.08 mol L^{-1}) and 2-MIM (1.3 mol L^{-1}) solutions. The prepared CNWs@M fabric was first soaked in 50 mL of 2-MIM aqueous solution for 1 h, then different volumes of Zn^{2+} solution were added (with 2-MIM to Zn^{2+} molar ratios of 4:1, 8:1, 12:1, 16:1, and 32:1 respectively) and shaken (90 rpm) at 50 °C for 2 h to promote the in-situ growth of ZIF-8 [34]. The as-obtained CNWs@M/ZIF-8 samples were alternately washed three times with DI water and ethanol (95 wt%) to remove unreacted precursors and suspended ZIF-8 particles. The resulting CNWs@M/ZIF-8 textiles were subjected to overnight vacuum drying at a temperature of 25 °C.

2.4. Oxidation test of CNWs@M and CNWs@M/ZIF-8

The CNWs@M and CNWs@M/ZIF-8 fabrics (50×50 mm) were exposed to 95 °C/95 % RH (relative humidity) for varied periods (1, 7, 15, and 30 days) in order to conduct a high-temperature oxidation test. The textiles were briefly taken out from the chamber to measure their EMI shielding performance and returned after measurement.

2.5. Antibacterial activity assessments

The antibacterial activity of samples was quantified using a colony counting technique. Representative strains of *Escherichia coli* (*E. coli*) (ATCC 8739) and *Staphylococcus aureus* (*S. aureus*) (ATCC 29213) were used as harmful microorganisms. Bacteria were grown overnight at 37 °C and 200 rpm in Luria-Bertani broth. The bacterial suspensions were diluted to a concentration of 5×10^6 CFU/mL for various antibacterial tests. For the colony counting method, The CNWs@M/ZIF-8 textiles (8×10 mm^2) and 0.2 mL of the diluted bacterial suspension were transferred to a sterilized glass vial containing 1.8 mL of LB broth. Subsequently, the mixed system was incubated at 37 °C and 200 rpm on a shaker for various durations. Ultimately, 0.1 mL of the resulting mixture was distributed onto LB agar plates and incubated at 37 °C for 24 h prior to counting.

Visual assessment of inhibition zones was conducted to evaluate the release effect of CNWs@M samples on the growth of *E. coli* and *S. aureus* strains. Firstly, the strains were revived, and then 100 μL of the revived bacterial suspension (5×10^8 CFU/mL) was evenly spread on LB agar plates. Subsequently, CNWs@M and CNWs@M/ZIF-8 samples (diameter: 9 mm), sterilized by ultraviolet irradiation for 30 min, were placed on the agar plates inoculated with bacteria and incubated at 37 °C for 24 h. Finally, the size of inhibition zones was measured to quantify the release effect. For the photodynamic/photothermal antibacterial test, 0.1 mL of the prepared bacterial suspension and 8×10 mm^2 of the CNWs@M/ZIF-8 textile were irradiated in a 6-well plate under NIR (808 nm) laser at different light energy densities for different times. Subsequently, 1.9 mL of LB broth was added to the mixed system of bacterial suspension and samples, and bacterial elution was facilitated through agitation and vortexing. 0.1 mL of the suspension was spread onto a solid culture medium, followed by culturing at 37 °C for 24 h. Afterwards, the surviving colonies were counted. The antibacterial efficiency (AE) and the survival rate (SR) were calculated using formulas AE = (B-A)/B x 100 % and SR = A/B x 100 % (A: the number of colonies in the experimental group, B: the number of colonies in the control group).

To observe the changes in the morphology of the bacterial cell membrane, the bacteria were centrifuged at 4075 *g* (rcf) for 5 min, washed with SPSS solution three times, and fixed with 4 % glutaraldehyde at 4 °C for 8 h. A series of ethanol concentrations (20–100 %) were used to dehydrate microorganisms, which were then dried overnight at room temperature and observed by scanning electron microscopy.

2.6. Characterization

The morphologies of MXene, ZIF-8, and CNWs@M/ZIF-8 were observed using a scanning electron microscope (SEM, Hitachi Regulus 8100, Japan). The structural morphology of MXene (Ti$_3$C$_2$T$_X$) was observed using a transmission electron microscope (TEM, JEOL Jem 2100, Japan). X-ray diffraction spectra of the materials were collected using an X-ray diffractometer (XRD Ultima IV, K α Rigaku, 5° min^{-1}, Japan). The chemical composition and state of all prepared samples were analyzed using X-ray photoelectron spectroscope (XPS, AXIS Ultra DLD, Shimadzu, UK) and a VERTEX80v spectrometer (FT-IR Bruker Optik GmbH, Germany). Photothermal infrared thermal imaging photos were collected with an infrared camera (FOTRIC 223 s), and the prepared sample size was 8×10 mm^2. An environmental scanning electron microscope (ESEM, Quanta 200, FEI, USA) was used to examine the morphology of bacteria. A UV–Vis spectrophotometer (UV-1780, Shimadzu, Japan) and a microplate reader (Multiskan FC, Thermo Scientific, USA) were used to collect the absorbance of the samples.

The CNWs@M/ZIF-8 sample (8×10 mm^2) was immersed in DI H$_2$O and 100 μL of supernatant was extracted at predetermined time intervals (0.5, 1, 2, 3, 4, 6, 8, 10, 12 and 24 h) for Zn^{2+} detection (ICP-MS, JY2000–2, France), and an equal volume of DI H$_2$O was supplemented. With the utilization of a high-power NIR laser module (FU808ADX-F34, China) and a clean bench as the core, a NIR photodynamic antibacterial system with a controllable optical power density was constructed for PTT/PDT antibacterial experiments. All PTT/PDT antibacterial tests were conducted in a sterile and ultra-clean bench.

The EMI SE of the samples in the X-band (8.2–12.4 GHz) was collected by a vector network analyzer (Keysight N5247A). Among them, the calculation formula of the total SE is as follows:

$$R = |S_{11}|^2$$

$$T = |S_{21}|^2$$

$$A = 1 - R - T$$

$$SE_R = -log_{10}(1 - R)$$

$$SE_A = -log_{10}\left(\frac{T}{1 - R}\right)$$

$$SE_T = SE_A + SE_R$$

$$EMI\ Shielding\ Efficiency\ (\%) = 100 - 10^{-\frac{SE}{10}}$$

where SE_T, SE_A, and SE_R were total shielding, absorption, and reflection effectiveness[dB], respectively.

3. Results and discussion

3.1. Preparation and characterization of MXene and ZIF-8

In accordance with previously reported methods, MXene (Ti$_3$C$_2$T$_X$) nanosheets were synthesized using a hydrofluoric acid etching approach, as illustrated in Fig. 1a. Briefly, HCl/LiF was employed to etch the precursor MAX (Ti$_3$AlC$_2$) powder (Fig. S1), removing the Al layer to yield multilayered MXene (Fig. 1b). Subsequently, the obtained multilayered MXene, featuring accordion-like structures (Fig. 1b), was subjected to ultrasonication for exfoliation, resulting in single-layer or few-

layers MXene nanosheets. TEM images of the MXene nanosheets revealed well-defined edges and intact morphological structures (Fig. 1c). The X-ray diffraction (XRD) patterns (Fig. S2) exhibited the characteristic peak of $Ti_3C_2T_X$ at 7°, confirming the successful etching of MAX. Furthermore, the colloidal dispersion of MXene nanosheets displayed the pronounced Tyndall scattering effects in Fig. S3, a distinctive feature of uniform colloidal dispersions. Collectively, these results validate the successful preparation of single-layer or few-layers MXene sheets.

To achieve a complete zeolitic imidazolate framework (ZIF-8) with antimicrobial properties, we improved the conventional preparation method as depicted in Fig. 1d. SEM images of ZIF-8 synthesized using different 2-MIM/Zn^{2+} molar ratios are shown in Fig. S4. The results indicated that ZIF-8 obtained with a 2-MIM/Zn^{2+} molar ratio smaller than 12:1 exhibited a carambola structure, lacking a distinct zeolitic appearance. However, ZIF-8 synthesized with molar ratios of 16:1 and 32:1 displayed a complete zeolitic structure with uniform particle sizes. Moreover, antimicrobial assays (Fig. S5) demonstrated that ZIF-8 synthesized with a 32:1 M ratio exhibited antibacterial efficiencies of 58.71 % and 62.97 % against *E. coli* and *S. aureus*, respectively, while molar ratios of 16:1 and below achieved antibacterial efficiencies exceeding 99.99 %. Therefore, the optimal 2-MIM/Zn^{2+} molar ratio for ZIF-8 synthesis was determined to be 16:1. Fig. 1e illustrates a representative SEM image of ZIF-8 with an average lateral size of approximately 1.13 ± 0.31 μm (count: 100) (Fig. S6). Furthermore, XRD patterns exhibited characteristic crystal diffraction peaks corresponding to the (011), (002), (112), and (222) planes at 7.3°, 10.4°, 12.7°, and 18.5°, respectively (Fig. 1f), confirming the successful synthesis of ZIF-8 with intact crystal facets.

3.2. Surface engineering of cellulose nonwovens

Exactly, we aimed at creating a straightforward and viable method for producing smart textiles [43]. The resulting smart textiles not only exhibit excellent PTT/PDT synergistic antibacterial effects when exposed to NIR light, but also gradually release antibacterial agents to achieve antibacterial objectives, thereby catering to various challenging working environments. Although smart textiles were extensively manufactured and utilized across various fields, developing textiles with controlled release of antibacterial agents and high-performance PTT/PDT synergistic antibacterial properties remains a formidable challenge. In this context, we established an efficient surface engineering strategy and an in-situ growth process that enables the continuous fabrication of layer-by-layer assembled structures with controlled release of antimicrobial agents and high-performance PTT/PDT synergistic antibacterial effects. As illustrated in Fig. 2a, layers of highly conductive and efficient NIR-responsive MXene were achieved through the repeated spray assembly of MXene dispersion. The typical morphologies of CNWs are depicted in SEM images (Fig. 2b-d). Given the abundant -OH groups on the surface of cellulose-based fibers of CNWs and MXene sheets, a strong connection is formed through hydrogen bonding interactions, as depicted in Fig. 2e-g. The cross-sectional SEM image of CNWs@M (Fig. 2g) indicated that MXene nanosheets were firmly incorporated onto the surface of cellulose fiber, forming a thin layer. The grooves and indentations formed by stacking of MXene (Fig. 2e and f) provide a larger specific surface and interface area for the in-situ growth of MOF layer (ZIF-8). The prepared CNWs@M textile was immersed in 2-MIM solution for 1 h, and after the addition of Zn^{2+}, a continuous layer of ZIF-8 with a thickness around 500 nm was grown on the surface of
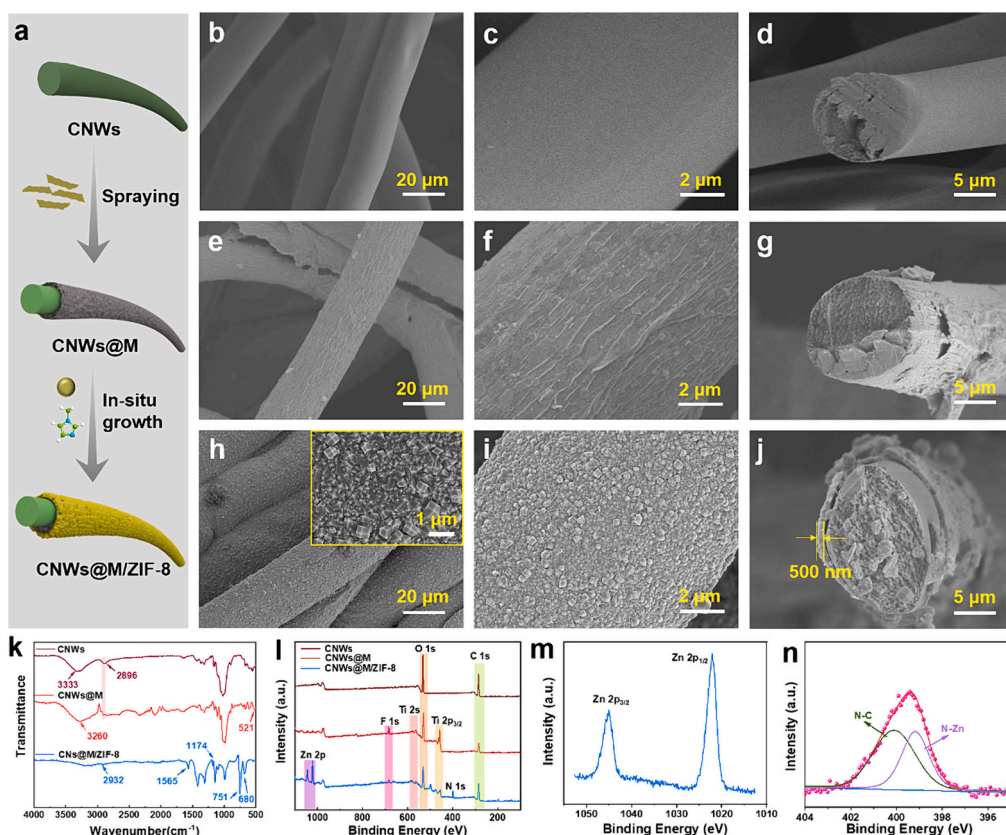
Fig. 2. Surface engineering and characterization of CNWs@M/ZIF-8. (a) The schematic representation of the synthetic procedure for CNWs@M/ZIF-8, including MXene loading and in situ growth of ZIF-8. SEM images of (b-d) CNWs, (e-g) CNWs@M, and (h-j) CNWs@M/ZIF-8 (9.5 mm × 2.0 K, 9.5 mm × 5.0 K) (where d, g and j are cross-sectional SEM images of CNWs, CNWs@M, and CNWs@M/ZIF-8 (9.5 mm × 5.0 K)). The inset is a partially enlarged SEM image of ZIF-8 (9.5 mm × 20.0 K). (k) FTIR spectra of CNWs, CNWs@M and CNWs@M/ZIF-8. (l) Wide scan XPS spectra of CNWs, CNWs@M and CNWs@M/ZIF-8. (m) Zn 2p core-level and (n) N 1 s core-level spectra of CNWs@M/ZIF-8.

CNWs@M (Fig. 2h-j). The reason for selecting ZIF-8 among various MOF materials is its pore size of approximately 3.4 Å, which effectively prevents the contact of MXene layers with water molecules, thereby hindering the induced oxidation of MXene. As shown in Fig. 2h and i, the in-situ grown ZIF-8 on the CNWs@M surface exhibited a continuous and intact morphological feature, whereas the in-suit grown ZIF-8 layer on CNWs surface without MXene coating (Fig. S7) showed obvious fragmentation and detachment. This is possibly attributed to effectively reducing the rigidity of the ZIF-8 layer and enhancing the binding between the ZIF-8 layer and the fibers by introducing flexible MXene layers. Simultaneously, the elemental mapping of CNWs@M/ZIF-8 (Fig. S8) shows a uniform distribution of C, N, Ti, and Zn elements, confirming the successful loading of MXene and ZIF-8. SEM images after 10 min of ultrasonic cleaning of CNWs@M/ZIF-8 (Fig. S9a) and CNWs/ZIF-8 (Fig. S9b) indicated severe fragmentation and detachment of the ZIF-8 layer in CNWs/ZIF-8, while the ZIF-8 layer in CNWs@M/ZIF-8 retained its integrity. This further confirms that the flexible MXene layer enhanced the mechanical strength of the ZIF-8 layer. Additionally, the folding and curling optical images of CNWs@M/ZIF-8 demonstrated the flexibility of the smart textile (Fig. S10). These advantages provided substantial potential for practical applications of the as-developed smart textiles in daily life.

Subsequently, the composite materials formed during the layer-by-layer assembly process of the smart textiles (CNWs@M/ZIF-8) were further characterized with FT-IR (Fig. 2k). As can be seen, CNWs showed typical peaks of natural cellulose fibers near 3333 cm^{-1} (-OH stretching) and 2896 cm^{-1} (C—H stretching). Comparing to CNWs, the FT-IR spectrum of CNWs@M exhibited a characteristic peak of MXene around 521 cm^{-1} (Ti—O) and the -OH peak at 3333 cm^{-1} (CNWs) shifted towards around 3260 cm^{-1} (CNWs@M), confirming the successful incorporation of MXene onto the CNWs surface through hydrogen bonding [44]. Upon ZIF-8 assembly, the infrared spectrum of CNWs@M/ZIF-8 textile exhibited characteristic absorption peaks at

680, 751, and 1174 cm^{-1}, attributing to the vibrations of Zn—O, Zn—N, and C–OH bonds. Furthermore, the vibrational absorption bands of the C—H (1565 cm^{-1}) and C—N (2932 cm^{-1}) bonds of the ZIF-8 ligand 2-MIM were observed (Fig. 2k) [45]. These findings confirmed the successful loading of ZIF-8 onto CNWs@M. XPS analysis was employed to ascertain the surface chemical changes during the assembly process of CNWs@M/ZIF-8 textiles (Fig. 2I). For the CNWs@M textiles (Fig. 2I), three new peaks at 458.8 eV, 565.7 eV, and 683.8 eV were attributed to Ti 2P$_{3/2}$, Ti 2P$_{3/2}$, and F 1S, respectively. Subsequent to the in-situ growth of ZIF-8 (Fig. 2I and m), three new peaks were observed at 1021.5 eV (Zn 2P$_{3/2}$) and 1044.6 eV (Zn 2P$_{1/2}$), attributable to Zn 2P, along with a peak at 399.6 eV (N 1 s), indicating the presence of ZIF-8. In addition, the N 1S core-level spectra of CNWs@M/ZIF-8 could be deconvoluted into two characteristic peaks at 399.2 eV (Zn—N) and 400.1 eV (—NH$_2$) (Fig. 2n). These results further confirmed the successful incorporation of both MXene and ZIF-8 layers [28,34,45].

3.3. Photothermal and photodynamic properties of CNWs@M/ZIF-8

It is widely acknowledged that MXene possesses exceptional photothermal conversion capability and photodynamic activity via NIR radiation, which is significant for the advancement of potential applications in smart light-driven antibacterial wearable textiles. Therefore, we investigated the PTT/PDT activity of the as-prepared CNWs@M/ZIF-8 textile. Fig. 3a shows the temperature (central maximum) evolution of CNs@M/ZIF-8 illuminated with 808 nm NIR perpendicular to smart textiles at different power densities. It was evident that the temperature of the CNWs@M/ZIF-8 textile quickly reached the saturation temperature and remains stable, indicating that the light-to-heat conversion of these cellulose-based smart textiles was sensitive and stable. Furthermore, the temperature gradually increased with increasing NIR power, exhibiting efficient photothermal conversion behavior. Prolonging infrared laser duration at 200 mW cm^{-2} optical power density as well as
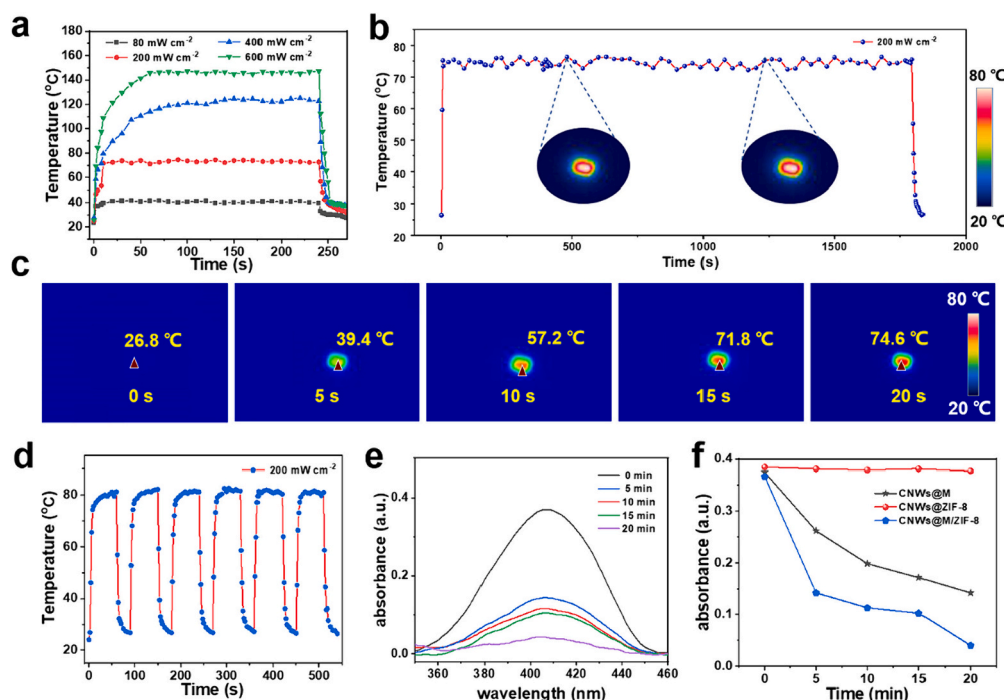
Fig. 3. Photothermal/photodynamic performance of the CNWs@M/ZIF-8. (a) Temperature profiles of the CNWs@M/ZIF-8 under a stepwise power density from 80 to 600 mW cm^{-2} (MXene content: 1.46 mg cm^{-2}, 8 × 10 mm^2). (b) photothermal stability of CNWs@M/ZIF-8 under a 200 mW cm^{-2} input optical power density for 2000 s. (c) Infrared thermographic photographs of CNWs@M/ZIF-8 under 808 nm NIR irradiation (200 mW cm^{-2}) at different time intervals. (d) Temperature-time curve of CNWs@M/ZIF-8 under the irradiation of simulated sunlight source for 6 cycles. (e) Time dependent UV–vis spectrum of DPBF with the CNWs@M/ZIF-8 textile under 808 nm NIR irradiation. (f) Decay curves of the DPBF absorption density at 410 nm with the ROS generation in acetonitrile under 808 nm NIR illumination.

temperature changes in cyclic heating were tested to evaluate the heating stability of smart textiles (Fig. 3b and c). Interestingly, the temperature of the CNWs@M/ZIF-8 rapidly increased to 74.6 °C within 20 s and remained stable at this temperature even after continuous irradiation for >2000 s, indicating its excellent long-term heating reliability. Furthermore, the CNWs@M/ZIF-8 demonstrated good stability over 6 heating cycles (Fig. 3d). The infrared irradiation images of CNWs@M/ZIF-8 with different MXene loading amounts (Fig. S11) show that with the continuous increase of MXene loading amount (0.30–2.23 mg cm^{-2}), the temperature rises from 23.7 to 95.7 °C, indicating that it is feasible to easily achieve controllable photothermal response behavior.

To further explore the photodynamic activity of the CNWs@M/ZIF-8 textile, the generation of singlet oxygen (O$_2$) under NIR radiation (808 nm, 300 mW cm^{-2}) was measured by 1,3-diphenylisobenzofuran (DPBF). In the presence of ^{1}O$_2$ molecules, the DPBF exhibited a decrease in the maximum absorption at 410 nm. As depicted in Fig. 3e, upon exposure to NIR 808 nm (300 mW cm^{-2}), the absorbance at 410 nm of the DPBF system experienced a significant decrease after 5 min, and declined by 85 % after 20 min. As shown in Fig. 3f, the absorbance of DPBF exposed to CNWs@M and CNWs@M/ZIF-8 both significantly decreased at 410 nm, with the latter showing a stronger decline than the former. However, CNWs/ZIF-8 did not cause a decrease in the absorbance of DPBF at 410 nm. These results indicated that the ROS generation of CNWs@M/ZIF-8 assembled with M/ZIF-8 was higher than that of CNWs@M and CNWs@ZIF-8. The possible reasons for this phenomenon could be analyzed based on two mechanisms of PDT process. For the Type I PDT pathway, the interface between the assembled ZIF-8 and MXene in CNWs@M/ZIF-8 could promote intermolecular charge transfer by forming an in-built electric field, reducing the energy required for excitation and further stabilizing the excited state [28]. For the Type II PDT pathway, the zeolite structure of ZIF-8 can serve as an oxygen reservoir, improving the oxygen environment in the Type II process, and increasing the effective collision rate between molecular oxygen and the excited state, thereby enhancing the ROS production [40].

3.4. Biocidal performance of CNWs@M/ZIF-8

Given the sustained and gradual release of Zn^{2+} from the ZIF-8 layer in an aqueous system, the CNWs@M/ZIF-8 textile is expected to have excellent antibacterial properties [46–48]. To verify this, the antibacterial properties of CNWs@M/ZIF-8 was examined using plate counting and inhibition zone assays. Representative Gram-negative bacterial (*E. coli*) and Gram-positive bacterial (*S. aureus*) strains were chosen as model microorganisms to assess the antibacterial activity of various composite layers fabricated during the process. Fig. S12a and S12b illustrate the time-dependent variation in killing efficiency of different composite layers against the two bacterial strains. The results indicated that within the first 5 mins, the antibacterial efficiency of all tested samples against *E. coli* and *S. aureus* were both below 24.38 %, suggesting that rapid bacterial killing was challenging for the material. However, after the sample exposed to bacterial suspension for 2 h, CNWs and CNWs@M without assembled ZIF-8 exhibited antibacterial efficiencies below 60.67 % for both bacterial strains, whereas CNWs@M/ZIF-8 achieved antibacterial efficiencies of 91.33 % and 94.02 % against *E. coli* and *S. aureus*, respectively. The inhibition zone test results (Fig. S14) indicated that there were no distinct inhibition zones observed after 24 h of CNWs@M contact with *E. coli* and *S. aureus*, whereas notable inhibition zones (total diameter: approximately 13 mm) emerged upon the introduction of the ZIF-8 layer. Simultaneously, it was observed that CNWs@M/ZIF-8 can continuously release Zn^{2+} in DI water (Fig. S13), reaching 0.67 ppm within 24 h and stabilizing, further demonstrating the significant sustained release characteristics of Zn^{2+}. Therefore, The formation of inhibition zones is attributed to ZIF-8 releasing Zn^{2+} due to electrostatic interactions with

bacterial pathogens, leading to bacterial growth inhibition or death by inducing cell deformation, rupture of the cell wall leading to cytoplasm leakage, and creation of an alkaline microenvironment [46,49]. To further evaluate the enduring antibacterial capacity of CNWs@M/ZIF-8, different samples were subjected to 24 and 48 h of treatment with *E. coli* and *S. aureus*, followed by dilution and plating of bacterial suspensions. As shown in Fig. S15a and S15b, the percentage of killed bacteria correspondingly increased with the incorporation of the ZIF-8 layer, while the original CNWs displayed no antibacterial effects against *E. coli* and *S. aureus*. In the case of *E. coli*, CNWs@M/ZIF-8 killed approximately 7 logs (24 h) and 7 logs (48 h) of bacterial cells, while CNWs/ZIF-8 killed <6 logs (24 h) and 6 logs (48 h) of bacterial cells. For *S. aureus*, CNWs@M/ZIF-8 respectively killed about 6 logs (24 h) and 7 logs (48 h) of bacterial cells, whereas CNWs/ZIF-8 killed approximately 5 logs (24 h) and 6 logs (48 h) of *S. aureus*. These results emphasized that the introduction of the ZIF-8 layer endows CNWs@M/ZIF-8 with exceptional antibacterial efficacy, allowing for sustained inhibition of bacterial proliferation. However, the challenge of effectively killing bacteria within a short timeframe remains to be addressed.

To tackle this challenge, the current study incorporates MXene (Ti$_2$C$_3$T$_x$) with exceptional photothermal and photodynamic properties into textile substrates [50,51]. The excellent photothermal and photodynamic properties provided the possibility to extend the applications of the CNWs@M/ZIF-8 to PTT/PDT antibacterial [52]. As shown in Fig. 4a-c, *E. coli* and *S. aureus* were co-cultured with different loading-MXene contents of CNWs@M/ZIF-8 under 808 nm laser irradiation (300 mW cm^{-2}) for 10 min while the control group was left untreated. Antibacterial efficiency of the samples was carried out through the colony counting method. After exposure to the NIR laser (NIR+), when the loading contents of MXene was 1.46 mg cm^{-2}, the antibacterial efficiency of CNWs@M/ZIF-8 against the *E. coli* and *S. aureus* reached 99.99 %, suggesting that the MXene loading is essential for the effective PTT/PDT performance. In the group without NIR (NIR-) irradiation, CNWs@M/ZIF-8 showed no significant antibacterial activity. To further investigate the PTT/PDT antibacterial properties of the samples, the impact of optical power density (Fig. 4d and e) and irradiation duration (Fig. S16) on the antibacterial efficiency of the samples was explored. The results demonstrated a positive correlation between the bactericidal efficiency of CNWs@M and CNWs@M/ZIF-8 against *E. coli* and *S. aureus* and optical power density as well as irradiation time. Compared to CNWs@M, CNWs@M/ZIF-8 exhibited higher bacterial killing efficiency when irradiated at light power densities below 300 mW cm^{-2} (808 nm) for 5 min (Fig. 4d, e, and S16), further confirming the ability of the ZIF-8 layer to promote thermal therapy and ROS generation. Additionally, at light power densities above 300 mW cm^{-2} (Fig. 4d and e) and irradiation time exceeding 5 min (Fig. S16), CNWs@M/ZIF-8 achieved a bacterial killing efficiency above 99.99 % against both *E. coli* and *S. aureus*. Therefore, NIR laser (808 nm) irradiation with light intensity of 300 mW cm^{-2} was fixed for effective bacterial deactivation in our work, which is below the MPE limit to skin and tissue [33]. As depicted in Fig. 4f and h, the co-culture of CNWs@M/ZIF-8 and bacteria (5 × 10^6 CFU/mL) was subjected to irradiation at an optical power density of 300 mW cm^{-2} for 1 to 5 min, followed by survival rate calculation using the plate counting method. Not surprisingly, the bacteria stayed alive on CNWs@M/ZIF-8 in the dark environment (Fig. 4f), and their survival rate exceeded 85.7 %. After being exposed to the NIR irradiation, the origin CNWs exhibited no evident bactericidal performance, illustrating that the sole NIR treatment hardly induced an antibacterial effect. However, the bacterial colony counts upon contact with CNWs@M/ZIF-8 initially decreased with time, reaching near-zero survival rates for both *E. coli* and *S. aureus* after an irradiation duration of 5 min (Fig. 4h). Cycling PTT/PDT antibacterial tests of CNWs@M/ZIF-8 were conducted to assess their stability and reproducibility in practical applications. As shown in (Fig. 4i), the antibacterial efficiency against *E. coli* and *S. aureus* was both >94.2 % after 5 cycles. These results indicated that the reusable of CNWs@M/ZIF-8 textiles materials
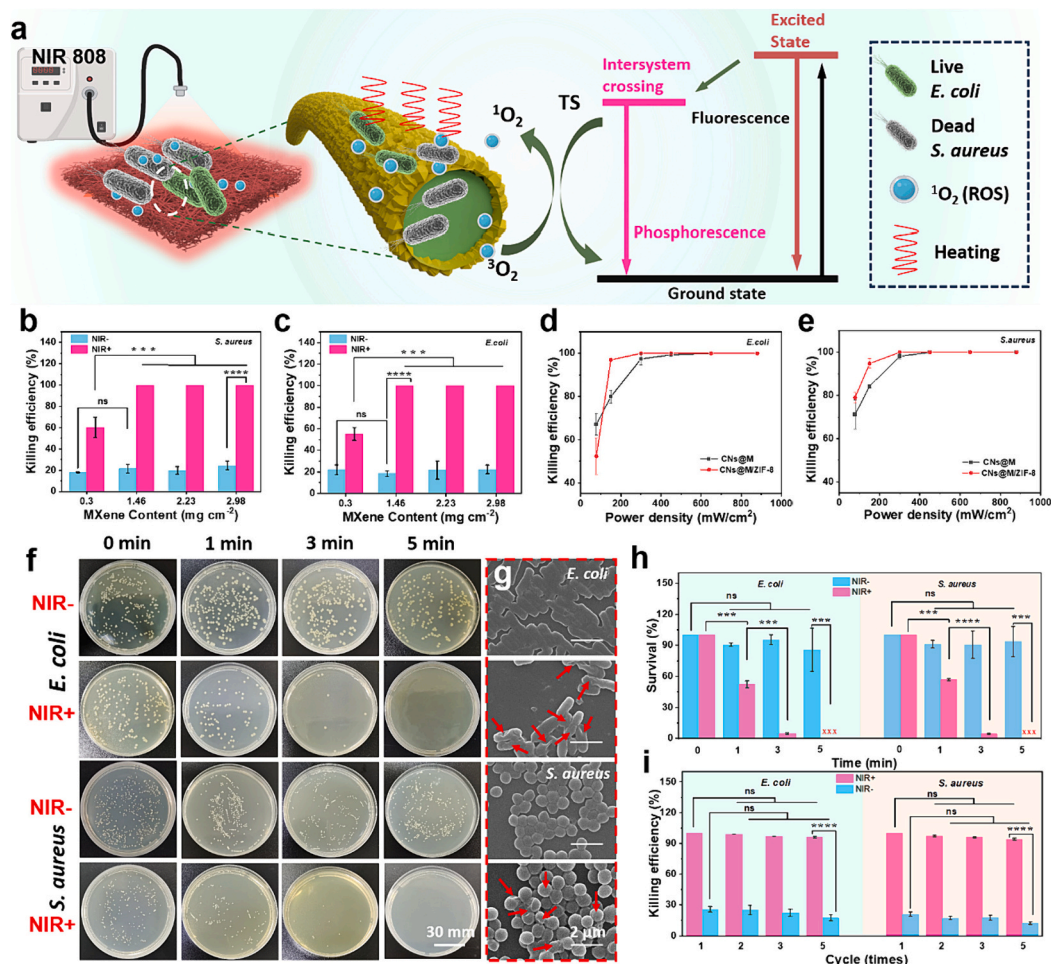
Fig. 4. Antibacterial capability of CNWs@M/ZIF-8. (a) Schematic illustration of the PTT/PDT antibacterial properties of the CNWs@M/ZIF-8. Bactericidal activity of CNWs@M/ZIF-8 with different MXene loadings (0.3–2.98 mg cm^{-2}) against (b) *E. coli* and (c) *S. aureus* under dark and 808 nm NIR laser (300 mW cm^{-2}) (ns>0.9999, ***$p < 0.001$, ****$p < 0.0001$, $n = 3$). Bactericidal activity of CNWs@M and CNWs@M/ZIF-8 against (d) *E. coli* and (e) *S. aureus* at the different optical power density (808 nm NIR laser) (n = 3). (f) Optical photos of *E. coli* and *S. aureus* after cocultured with CNWs@M/ZIF-8 at different times under dark and 808 nm NIR laser (300 mW cm^{-2}) (n = 3). (g) SEM images of *E. coli* and *S. aureus* after corresponding treatment for 5 min (n = 3). (h) Corresponding statistical analysis of the bacterial viability. (i) PTT/PDT antibacterial efficiency of CNWs@M/ZIF-8 for 5 cycles (ns > 0.9999, ***p < 0.001, ****p < 0.0001, n = 3).

achieved rapid and efficient bactericidal treatment through synergistic PTT/PDT effects. As widely known, the antibacterial strategy of personal protective clothing often requires exposure to ultraviolet (UV) light for over 30 min [53], which usually failed to achieve rapid and efficient bacterial killing. Notably, the smart textile CNWs@M/ZIF-8 demonstrates the ability to effectively eliminate pathogens within 5 min under NIR irradiation with low light energy density. Moreover, the smart textile can maintain the sustained inhibition of bacterial proliferation through the gradual release of Zn^{2+} in work environments where NIR irradiation is not feasible. This novel smart textile, employing a synergistic combination of various antibacterial strategies, is poised to become a strong contender for the next generation of diverse bio-protective garments.

To gain further insight into the antibacterial mechanism, the morphology of *E. coli* and *S. aureus* incubated on CNWs@M/ZIF-8 was further revealed during the various treatments (Fig. 4g). In the non-irradiated control group, a smooth and intact bacterial surface was observed, whereas on the bacteria subjected to infrared irradiation, distinct surface wrinkling, pore formation, and rupture became clearly visible. The rapid changes on the surface of *E. coli* and *S. aureus* were mainly caused by the high temperature and ROS induced by CNWs@M/ZIF-8 [28,44]. Fig. 4a illustrates the energy transfer mechanism for $^1O_2$ generation. When CNWs@M/ZIF-8 was illuminated, its photosensitizer

M/ZIF-8 absorbed energy and formed an excited singlet state, followed by possible fluorescence emission or intersystem crossing, generating the excited triplet state (TS) of M/ZIF-8. Ultimately, the excited triplet state of M/ZIF-8 may emit phosphorescence or react with triplet oxygen ($^3O_2$) to generate $^1O_2$ which could damage bacterial cells via peroxidation of lipids and carbonylation of proteins [28,54,55]. Furthermore, in comparison to *E coli*, there was a significantly lower occurrence of surface wrinkling in *S aureus*, attributed to the thicker cell wall of *S. aureus* (Gram-positive bacteria), which serves as an impediment during the PTT/PDT process [56,57].

3.5. Electromagnetic interface shielding performance of CNWs@M/ZIF-8

With the advent of the 5G era, the issue of electromagnetic wave pollution from various smart portable electronic products has become increasingly prominent, posing safety hazards to human health and the surrounding environment. Considering the wearable electronic products are often in direct or indirect contact with human body in their operational scenarios, there is an urgent need to develop wearable protective materials with excellent EMI shielding performance. It was noteworthy that the introduction of MXene-loaded CNWs imparted remarkable PTT/PDT antibacterial properties to smart textiles which surface and interfacial areas were also increased. The highly conductive MXene layer

reflected a significant portion of incident electromagnetic waves, while the remaining incident waves were further absorbed and dispersed after multiple reflections within the disordered and intricate multi-porous structure and a multi-layer MXene core-shell structure of the CNWs@M/ZIF-8 textile material (Fig. 5a) [44,58,59]. The EMI shielding performance of the smart textiles could be tailored by varying MXene loading amounts, as shown in Fig. 5b, i.e., the EMI shielding properties of CNWs@M/ZIF-8 was closely related to MXene loading in the X-band frequency range (8.2–12.4 GHz). The EMI SE_T of the smart textiles increased gradually from 9.5 to 47.7 dB in the entire X-band as MXene loading increased from 0.3 to 2.98 mg cm^{-2}. Simultaneously, the EMI reflection (SE_R) and absorption (SE_A) values of the smart textiles similarly increased with the augmentation of MXene loading, as depicted in Fig. S17a and S17b. Encouragingly, the EMI SE of smart textiles increased to 47.7 dB when the MXene loading amount reached 2.98 mg cm^{-2} (Fig. 5c), with a high value of the EMI shielding efficiency approaching 99.99 % (Fig. S18), proving the outstanding EMI shielding effects delivered by the textiles loaded with MXene layers. Based on the trend of SE value variations, the EMI shielding performance could be easily controlled within the range of 9.5 to 47.7 dB. To broaden the controllable range of EMI shielding performance, an EMI shielding platform with 1 to 4 layers of CNWs@M/ZIF-8 was established. As shown in Fig. 5d, when the number of CNWs@M/ZIF-8 textile layer was increased from 1 to 4, the EMI shielding performance increased from 47.7 to 88.2 dB, effectively expanding the control range to 9.5–88.2 dB. Furthermore, a comparison between the smart textiles and reported advanced EMI shielding materials is presented in Fig. 5e and Table S1, including textiles based on carbon nanotubes, graphene, metals, and

MXene. Clearly, the smart textiles developed in the current work exhibited the highest absolute shielding effectiveness per unit thickness (EMI SE/thickness) at lower thickness, indicating its superiority over those reported elsewhere and positioning it as a potential next-generation flexible EMI shielding material.

To demonstrate the enhanced stability of CNWs@M/ZIF-8 textiles, their electromagnetic shielding effectiveness (EMI SE) under harsh environmental conditions was investigated, as shown in Fig. 5f. The EMI SE performance of CNWs@M textile loaded with 2.98 mg cm^{-2} of MXene was evaluated in the X-band (8.2–12.4 GHz), a shielding effectiveness of 52.6 dB and a shielding efficiency of 99.99 % were achieved (Fig. S19a and S19b). Subsequently, CNWs@M textiles were exposed to harsh conditions at 95 °C and 95 % relative humidity (RH) for up to 30 days, simulating oxidative degradation. Under such conditions, the EMI shielding performance of CNWs@M textiles was significantly deteriorated, with reductions in shielding effectiveness to 46.3, 41.0, and 26.8 dB after 7, 15, and 30 days, respectively. In contrast, CNWs@M/ZIF-8 textiles exhibited an EMI SE of 47.2 dB in the X-band, and the values for textiles oxidized for 7, 15, and 30 days were well maintained at 43.3, 38.7, and 33.7 dB, respectively (Fig. 5g). Although the initial EMI SE of CNWs@M was slightly higher than that of CNWs@M/ZIF-8, the EMI SE of CNWs@M/ZIF-8 textiles was higher than that of CNWs@M after 30 days of oxidation under harsh conditions with the reduction of 28.6 % vs CNWs@M with a decrease of 49.0 % (Fig. S20). Evidently, the rate of decrease in EMI SE of CNWs@M was higher than that of CNWs@M/ZIF-8 under harsh environmental conditions. The results indicated that the in-situ grown ZIF-8 layer effectively inhibited the degradation of MXene incorporated in the textiles.
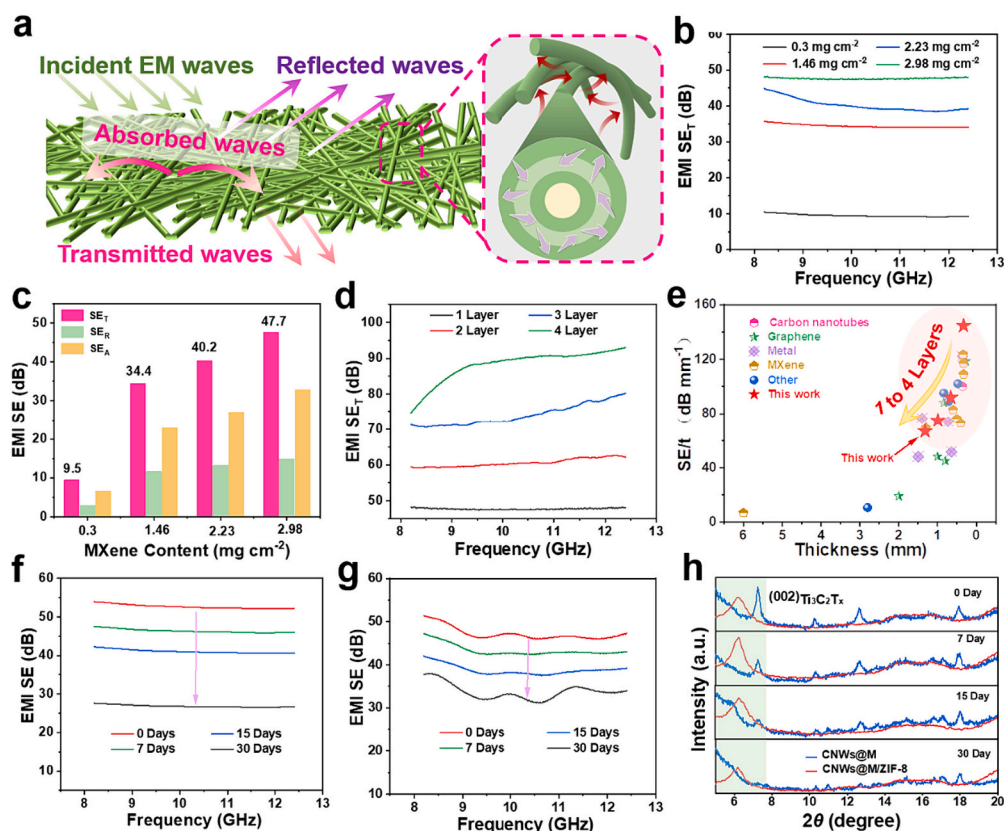
Fig. 5. EMI shielding performance of CNWs@M/ZIF-8. (a) EMI shielding mechanism of CNWs@M/ZIF-8. (b) SE_T of CNWs@M/ZIF-8 with different MXene loadings (0.3–2.98 mg cm^{-2}) under frequency of 8.2–12.4 GHz (X-band). (c) Average SE_R, SE_A, and SE_T of CNWs@M/ZIF-8 with different MXene loadings at 8.2–12.4 GHz ($n = 3$). (d) SE_T of CNWs@M/ZIF-8 with different layers (1–4 layers). (e) Comparison of EMI SE per unit thickness and coating thickness of CNWs@M/ZIF-8 with those of other coatings on EMI shielding fabrics reported in the literature. EMI SE_T values of (f) CNWs@M and (g) CNWs@M/ZIF-8 textile in X-band range before and after treating films at 95 % RH and 95 °C for different times (0, 7, 15 and 30 days). (h) XRD patterns of CNWs@M and CNWs@M/ZIF-8 textile after exposure to certain environments (95 % RH and 95 °C) for 1, 7, 15, and 30 days.

Furthermore, to further demonstrate the enhanced stability of CNWs@M/ZIF-8 textiles, the XRD changes of CNWs@M and CNWs@M/ZIF-8 structures over different periods of exposure to the environment were tracked (only XRD spectra in the range of 5–20° are shown for a more effective tracking of MXene oxidation) (Fig. 5h). Comparing to CNWs@M, the (002) peak of CNWs@M/ZIF-8 shifted to a lower angle, indicating that the organic ligand and the central metal ions of ZIF-8 were spontaneously inserted into the MXene interlayer during the in-situ growth process. After 30 days of exposure, the (002) peak of CNWs@M completely disappeared, while the (002) peak of CNWs@M/ZIF-8 remained detectable. This suggested that the two-dimensional layered structure unprotected by the ZIF-8 layer experienced greater oxidation and disruption. This protective mechanism was likely due to the dense ZIF-8 protective layer partially obstructing oxygen and water from attacking MXene layer, thereby hindering the oxidation of MXene. Simultaneously, ZIF-8 precursor intercalates and passivates the defect sites and dangling bonds on MXene surface, further enhancing the chemical stability of the MXene layer [34].

4. Conclusion

A facile and efficient layer-by-layer assembly method was developed in this work to fabricate breathable, flexible and smart wearable antibacterial textiles in conjunction with the in-situ growth of ZIF-8 layers on MXene-loaded cellulose textiles for outstanding antibacterial and EMI shielding effectiveness. The presence of the MXene layer enhanced the interface interactions between the ZIF-8 layer and the textile fibers, imparting excellent PTT/PDT activity and EMI shielding performance to the material. The assembled MXene/ZIF-8 bilayer structure promoted ROS generation upon light irradiation and effectively prevented oxygen and water-induced oxidation of the MXene layer. The smart textile can rapidly eradicate pathogenic bacteria within 5 min of NIR (808 nm) irradiation. Simultaneously, under non-infrared light conditions, the gradually released Zn^{2+} from the ZIF-8 layer effectively inhibited bacterial proliferation within 48 h. Furthermore, EMI shielding efficiency (9.5–88.2 dB) of the smart textile can be readily adjusted by modulating the loading amount of MXene and the thickness of the smart textile. In summary, with the unique advantages of the simple and convenient assembly process and multi-functional integration, the smart textiles created in this work offer innovative biomedical and bioprotective materials for a variety of applications.

CRediT authorship contribution statement

Zhaochuan Yu: Writing – review & editing, Writing – original draft, Methodology, Formal analysis, Data curation, Conceptualization. **Chao Deng:** Writing – review & editing, Visualization, Supervision, Funding acquisition, Conceptualization. **Chenhui Ding:** Supervision, Software, Investigation. **Xing Zhang:** Supervision, Resources, Formal analysis. **Yuqian Liu:** Validation, Software, Funding acquisition, Data curation. **Chao Liu:** Writing – review & editing, Software, Funding acquisition, Formal analysis. **Zhichao Lou:** Supervision, Funding acquisition, Formal analysis. **Farzad Seidi:** Project administration, Methodology, Data curation. **Jingquan Han:** Visualization, Validation, Resources, Funding acquisition. **Qiang Yong:** Supervision, Resources, Funding acquisition, Conceptualization. **Huining Xiao:** Writing – review & editing, Supervision, Resources, Funding acquisition, Conceptualization.

Declaration of competing interest

The authors declare that they have no known competing financial interests or personal relationships that could have appeared to influence the work reported in this paper.

Data availability

Data will be made available on request.

Appendix A. Supplementary data

Supplementary data to this article can be found online at https://doi.org/10.1016/j.ijbiomac.2024.131080.

References

[1] F. Natalio, R. Fuchs, S.R. Cohen, G. Leitus, G. Fritz-Popovski, O. Paris, M. Kappl, H.-J. Butt, Biological fabrication of cellulose fibers with tailored properties, Science 357 (2017) 1118–1122, https://doi.org/10.1126/science.aan5830.
[2] G. Chen, Y. Li, M. Bick, J. Chen, Smart textiles for electricity generation, Chem. Rev. 120 (2020) 3668–3720, https://doi.org/10.1021/acs.chemrev.9b00821.
[3] Z. Zhao, K. Xia, Y. Hou, Q. Zhang, Z. Ye, J. Lu, Designing flexible, smart and self-sustainable supercapacitors for portable/wearable electronics: from conductive polymers, Chem. Soc. Rev. 50 (2021) 12702–12743, https://doi.org/10.1039/D1CS00800E.
[4] J.E. Ip, Wearable devices for cardiac rhythm diagnosis and management, Jama-j Am. Med. Assoc. 321 (2019) 337, https://doi.org/10.1001/jama.2018.20437.
[5] G. Chen, X. Xiao, X. Zhao, T. Tat, M. Bick, J. Chen, Electronic textiles for wearable point-of-care systems, Chem. Rev. 122 (2022) 3259–3291, https://doi.org/10.1021/acs.chemrev.1c00502.
[6] X. Shi, P. Chen, H. Peng, Making large-scale, functional, electronic textiles, Nature (2021), https://doi.org/10.1038/d41586-021-00945-9 d41586-021-00945–9.
[7] K. Zeng, X. Shi, C. Tang, T. Liu, H. Peng, Design, fabrication and assembly considerations for electronic systems made of fibre devices, Nat. Rev. Mater. 8 (2023) 552–561, https://doi.org/10.1038/s41578-023-00573-x.
[8] X.A. Zhang, S. Yu, B. Xu, M. Li, Z. Peng, Y. Wang, S. Deng, X. Wu, Z. Wu, M. Ouyang, Y. Wang, Dynamic gating of infrared radiation in a textile, Science 363 (2019) 619–623, https://doi.org/10.1126/science.aau 1217.
[9] J.M. Cole, G. Pepe, O.K. Al Bahri, C.B. Cooper, Cosensitization in dye-sensitized solar cells, Chem. Rev. 119 (2019) 7279–7327, https://doi.org/10.1021/acs.chemrev.8b00632.
[10] J. Qian, Q. Dong, K. Chun, D. Zhu, X. Zhang, Y. Mao, J.N. Culver, S. Tai, J. R. German, D.P. Dean, J.T. Miller, L. Wang, T. Wu, T. Li, A.H. Brozena, R.M. Briber, D.K. Milton, W.E. Bentley, L. Hu, Highly stable, antiviral, antibacterial cotton textiles via molecular engineering, Nat. Nanotechnol. 18 (2023) 168–176, https://doi.org/10.1038/s41565-022-01278-y.
[11] C. Deng, Z. Yu, F. Liang, Y. Liu, F. Seidi, Q. Yong, C. Liu, Y. Zhang, J. Han, H. Xiao, Surface nano-engineering of cellulosic textiles for superior biocidal performance and effective bacterial detection, Chem. Eng. J. (2023) 145492, https://doi.org/10.1016/j.cej.2023.145492.
[12] Q.-W. Wang, H.-B. Zhang, J. Liu, S. Zhao, X. Xie, L. Liu, R. Yang, N. Koratkar, Z.-Z. Yu, Multifunc- tional and water-resistant MXene-decorated polyester textiles with outstanding electromagnetic inter- ference shielding and joule heating performances, Adv. Funct. Mater. 29 (2019) 1806819 doi:10.1002/adfm.201806819.
[13] M.I. El-kaliuoby, A.M. Khalil, A.M. El-Khatib, N. Shehata, Antibacterial synergism of electrospun nanofiber mats functioned with silver nanoparticles and pulsed electromagnetic waves, Polym 13 (2021) 277, https://doi.org/10.3390/polym13020277.
[14] M. Farno, C. Lamarche, C. Tenailleau, S. Cavalié, B. Duployer, D. Cussac, A. Parini, B. Sallerin, S. Girod Fullana, Low-energy electron beam sterilization of solid alginate and chitosan, and their polyelectrolyte complexes, Carbohydr. Polym. 261 (2021) 117578, https://doi.org/10.1016/j.carbpol.2020.117578.
[15] X. He, L. Dai, L. Ye, X. Sun, O. Enoch, R. Hu, X. Zan, F. Lin, J. Shen, A vehicle-free antimicrobial polymer hybrid gold nanoparticle as synergistically therapeutic platforms for *Staphylococcus aureus* infected wound healing, Adv. Sci. 9 (2022) 2105223, https://doi.org/10.1002/advs.202105223.
[16] Z. Li, S. Chen, Y. Huang, H. Zhou, S. Yang, H. Zhang, M. Wang, H. Guo, J. Yin, Photoswitchable AIE photosensitizer for reversible control of singlet oxygen generation in specific bacterial discrimination and photocontrolled photodynamic killing of bacteria, Chem. Eng. J. 450 (2022) 138087 doi:10.1016/j.cej.2022.138087.
[17] A.A. Balhaddad, L. Mokeem, R. Alsahafi, M.D. Weir, H.H.K. Xu, M.A.S. Melo, Magnetic-based photosensitizer to improve the efficiency of antimicrobial photodynamic therapy against mature dental caries-related biofilms, MedComm-Biomater. Appli. 2 (2023) e67, https://doi.org/10.1002/mba2.67.

[18] N. Xu, X. Zhang, T. Qi, Y. Wu, X. Xie, F. Chen, D. Shao, J. Liao, Biomedical applications and prospects of temperature-orchestrated photothermal therapy, MedComm-Biomater. Appli. 1 (2022) e25, https://doi.org/10.1002/mba2.25.

[19] Y. Zou, S. Tao, J. Li, M. Wu, X. Zhou, Applications of nanomaterials as treatments and diagnostic biosensors in microbial infections, MedComm-Biomater. Appli. 2 (2023) e62, https://doi.org/10.1002/mba2.62.

[20] Y. Deng, X. Ouyang, J. Sun, X. Shi, Y. Li, Y.K. Chan, W. Yang, S. Peng, Rapid sterilisation and diabetic cutaneous regeneration using cascade bio-heterojunctions through glucose oxidase-primed therapy, Bioact. Mater. 25 (2023) 748–765, https://doi.org/10.1016/j.bioactmat.2022.07.003.

[21] A. Maleki, J. He, S. Bochani, V. Nosrati, M.-A. Shahbazi, B. Guo, Multifunctional photoactive hydrogels for wound healing acceleration, ACS Nano 15 (2021) 18895–18930, https://doi.org/10.1021/acsnano. 1c08334.

[22] N. Li, P. Zhao, D. Astruc, Anisotropic gold nanoparticles: synthesis, properties, applications, and toxicity, Angew. Chem. Int. Ed. 53 (2014) 1756–1789, https://doi.org/10.1002/anie.201300441.

[23] S. Liu, X. Tian, X. Zhang, C. Xu, L. Wang, Y. Xia, A green MXene-based organohydrogel with tunable mechanics and freezing tolerance for wearable strain sensors, Chinese Chem. Lett. 33 (2022) 2205–2211, https://doi.org/10.1016/j.cclet.2021.09.063.

[24] Z. Lu, F. Jia, L. Zhuo, D. Ning, K. Gao, F. Xie, Micro-porous MXene/aramid nanofibers hybrid aerogel with reversible compression and efficient EMI shielding performance, Compos. B Eng. 217 (2021) 108853, https://doi.org/10.1016/j.compositesb.2021.108853.

[25] M. Naguib, O. Mashtalir, J. Carle, V. Presser, J. Lu, L. Hultman, Y. Gogotsi, M. W. Barsoum, Two-Dimensional transition metal carbides, ACS Nano 6 (2012) 1322–1331, https://doi.org/10.1021/nn204153h.

[26] S. Tang, Z. Wu, G. Feng, L. Wei, J. Weng, E. Ruiz-Hitzky, X. Wang, Multifunctional sandwich-like composite film based on superhydrophobic MXene for self-cleaning, photodynamic and antimicrobial applications, Chem. Eng. J. 454 (2023) 140457, https://doi.org/10.1016/j.cej.2022.140457.

[27] B. Yan, M. Zhou, X. Liao, P. Wang, Y. Yu, J. Yuan, Q. Wang, Developing a multifunctional silk fabric with dual-driven heating and rapid photothermal antibacterial abilities using high-yield MXene dispersions, ACS Appl. Mater. Interfaces 13 (2021) 43414–43425, https://doi.org/10.1021/acsami.1c12915.

[28] S. Zhang, J. Ye, X. Liu, Y. Wang, C. Li, J. Fang, B. Chang, Y. Qi, Y. Li, G. Ning, Titanium carbide/zeolite imidazole framework-8/polylactic acid electrospun membrane for near-infrared regulated photothermal/photodynamic therapy of drug-resistant bacterial infections, J. Colloid Interface Sci. 599 (2021) 390–403, https://doi.org/10.1016/j.jcis.2021.04.109.

[29] F. Duan, Q. Jia, G. Liang, M. Wang, L. Zhu, K.J. McHugh, L. Jing, M. Du, Z. Zhang, Schottky junction nanozyme based on Mn-bridged co-phthalocyanines and $Ti_3C_2T_x$ nanosheets boosts integrative type I and II photosensitization for multimodal cancer therapy, ACS Nano 17 (2023) 11290–11308, https://doi.org/10.1021/acsnano.2c12270.

[30] A.K. Tareen, K. Khan, M. Iqbal, S. Golovynskyi, Y. Zhang, A. Mahmood, N. Mahmood, J. Long, A. Al-Ghamdi, C. Li, H. Zhang, Recent advances in MXenes: new horizons in biomedical technologies, Mater. Today Chem. 26 (2022) 101205, https://doi.org/10.1016/j.mtchem.2022.101205.

[31] M. Lan, S. Zhao, W. Liu, C. Lee, W. Zhang, P. Wang, Photosensitizers for photodynamic therapy, Adv. Healthc. Mater. 8 (2019) 1900132, https://doi.org/10.1002/adhm.201900132.

[32] X. Qin, Z. Wu, J. Fang, S. Li, S. Tang, X. Wang, MXene-intercalated montmorillonite nanocomposites for long-acting antibacterial, Appli. Surface Sci. 616 (2023) 156521, https://doi.org/10.1016/j.apsusc.2023.156521.

[33] D. Xi, M. Xiao, J. Cao, L. Zhao, N. Xu, S. Long, J. Fan, K. Shao, W. Sun, X. Yan, X. Peng, NIR light-driving barrier-free group rotation in nanoparticles with an 88.3% photothermal conversion efficiency for photothermal therapy, Adv. Mater. 32 (2020) 1907855, https://doi.org/10.1002/adma.201907855.

[34] E. Choi, J. Lee, Y.-J. Kim, H. Kim, M. Kim, J. Hong, Y.C. Kang, C.M. Koo, D.W. Kim, S.J. Kim, Enhanced stability of $Ti_3C_2T_x$ MXene enabled by continuous ZIF-8 coating, Carbon 191 (2022) 593–599, https://doi.org/10.1016/j.carbon.2022.02.036.

[35] Q. Qian, P.A. Asinger, M.J. Lee, G. Han, K. Mizrahi Rodriguez, S. Lin, F. M. Benedetti, A.X. Wu, W.S. Chi, Z.P. Smith, MOF-based membranes for gas separations, Chem. Rev. 120 (2020) 8161–8266, https://doi.org/10.1021/acs.chemrev.0c00119.

[36] J. Dong, X. Han, Y. Liu, H. Li, Y. Cui, Metal-covalent organic frameworks (MCOFs): a bridge between metal-organic frameworks and covalent organic frameworks, Angew. Chem. Int. Ed. 59 (2020) 13722–13733, https://doi.org/10.1002/anie.202004796.

[37] H.N. Abdelhamid, Zeolitic, imidazolate frameworks (ZIF-8) for biomedical applications: a review search results, CMC-Comput. mater. con. 28 (2021) 70237075, https://doi.org/10.2174/09298673286662106081 43703.

[38] H.S. Jhinjer, M. Jassal, A.K. Agrawal, Nanosized ZIF-8 based odor adsorbing and antimicrobial finish for polyester fabrics, Appli. Surface Sci. 639 (2023) 158153, https://doi.org/10.1016/j.apsusc.2023.158153.

[39] X. Li, M. Xu, Z. Geng, X. Xu, X. Han, L. Chen, P. Ji, Y. Liu, Novel pH-responsive CaO_2@ZIF-67-HA-ADH coating that efficiently enhances the antimicrobial, osteogenic, and angiogenic properties of titanium implants, ACS Appl. Mater. Interfaces 15 (2023) 42965–42980, https://doi.org/10.1021/acsami.3c08233.

[40] Z. Xie, X. Cai, C. Sun, S. Liang, S. Shao, S. Huang, Z. Cheng, M. Pang, B. Xing, A.A. A. Kheraif, J. Lin, O_2-loaded pH-responsive multifunctional nanodrug carrier for overcoming hypoxia and highly efficient chemo-photodynamic cancer therapy, Chem. Mater. 31 (2019) 483–490, https://doi.org/10.1021/acs.chemmater.8b04321.

[41] X. Zhao, A. Vashisth, J.W. Blivin, Z. Tan, D.E. Holta, V. Kotasthane, S.A. Shah, T. Habib, S. Liu, J.L. Lutkenhaus, M. Radovic, M.J. Green, pH, nanosheet concentration, and antioxidant affect the oxidation of $Ti_3C_2T_x$ and Ti_2CT_x MXene dispersions, Adv. Mater. Interfaces 7 (2020) 2000845 doi:10.1002/admi.202000845.

[42] V. Hoseinpour, Z. Shariatinia, Applications of zeolitic imidazolate framework-8 (ZIF-8) in bone tissue engineering: a review, Tissue Cell 72 (2021) 101588, https://doi.org/10.1016/j.tice.2021.101588.

[43] X. Li, J. Hao, R. Liu, H. He, Y. Wang, G. Liang, Y. Liu, G. Yuan, Z. Guo, Interfacing MXene flakes on fiber fabric as an ultrafast electron transport layer for high performance textile electrodes, Energy Storage Mater. 33 (2020) 62–70, https://doi.org/10.1016/j.ensm.2020.05.004.

[44] Z. Yu, C. Deng, F. Seidi, Q. Yong, Z. Lou, L. Meng, J. Liu, C. Huang, Y. Liu, W. Wu, J. Han, H. Xiao, Air-permeable and flexible multifunctional cellulose-based textiles for bio-protection, thermal heating conversion, and electromagnetic interference shielding, J. Mater. Chem. A 10 (2022) 17452–17463, https://doi.org/10.1039/D2TA04706C.

[45] J. Gao, L. Hao, R. Jiang, Z. Liu, L. Tian, J. Zhao, W. Ming, L. Ren, Surprisingly fast assembly of the MOF film for synergetic antibacterial phototherapeutics, Green Chem. 24 (2022) 5930–5940, doi:10.1039/D2GC00226D.

[46] M. Taheri, D. Ashok, T. Sen, T.G. Enge, N.K. Verma, A. Tricoli, A. Lowe, D. R. Nisbet, T. Tsuzuki, Stability of ZIF-8 nanopowders in bacterial culture media and its implication for antibacterial properties, Chem. Eng. J. 413 (2021) 127511, https://doi.org/10.1016/j.cej.2020.127511.

[47] Z. Liu, Y. Yi, S. Wang, H. Dou, Y. Fan, L. Tian, J. Zhao, L. Ren, Bio-inspired self-adaptive nano- composite array: from non-antibiotic antibacterial actions to cell proliferation, ACS Nano 16 (2022) 16549–16562, https://doi.org/10.1021/acsnano.2c05980.

[48] J. Chen, L. Song, F. Qi, S. Qin, X. Yang, W. Xie, K. Gai, Y. Han, X. Zhang, Z. Zhu, H. Cai, X. Pei, Q. Wan, N. Chen, J. Wang, Q. Wang, Y. Li, Enhanced bone regeneration via ZIF-8 decorated hierarchical polyvinylidene fluoride piezoelectric foam nanogenerator: coupling of bioelectricity, angiogenesis, and osteogenesis, Nano Energy 106 (2023) 108076, https://doi.org/10.1016/j.nanoen.2022.108076.

[49] Y.-W. Wang, A. Cao, Y. Jiang, X. Zhang, J.-H. Liu, Y. Liu, H. Wang, Superior antibacterial activity of zinc oxide/graphene oxide composites originating from high zinc concentration localized around bacteria, ACS Appl. Mater. Interfaces 6 (2014) 2791–2798, https://doi.org/10.1021/am4053317.

[50] S. Hao, H. Han, Z. Yang, M. Chen, Y. Jiang, G. Lu, L. Dong, H. Wen, H. Li, J. Liu, L. Wu, Z. Wang, F. Wang, Recent advancements on photothermal conversion and antibacterial applications over MXenes-based materials, Nano-Micro Lett. 14 (2022) 178, https://doi.org/10.1007/s40820-022-00901-w.

[51] X. He, Y. Qian, C. Wu, J. Feng, X. Sun, Q. Zheng, X. Li, J. Shen, Entropy-mediated high-entropy mxenes nanotherapeutics: NIR-II-enhanced intrinsic oxidase mimic activity to combat methicillin-resistant *staphylococcus aureus* infection, Adv. Mater. 35 (2023) 2211432, https://doi.org/10.1002/adma. 202211432.

[52] X. He, S. Koo, E. Obeng, A. Sharma, J. Shen, J.S. Kim, Emerging 2D MXenes for antibacterial applications: current status, challenges, and prospects, Coordi. Chem. Rev. 492 (2023) 215275, https://doi.org/10.1016/j.ccr.2023.215275.

[53] T. Dai, M.S. Vrahas, C.K. Murray, M.R. Hamblin, Ultraviolet C irradiation: an alternative antimicrobial approach to localized infections? Expert Rev. Anti-Infect. Ther. 10 (2012) 185–195, https://doi.org/10.1586/eri.11.166.

[54] X. Nie, X. Wu, A. Mensah, Q. Wang, F. Huang, Q. Wei, FRET as a novel strategy to enhance the singlet oxygen generation of porphyrinic MOF decorated self-disinfecting fabrics, Chem. Eng. J. 395 (2020) 125012, https://doi.org/10.1016/j.cej.2020.125012.

[55] C. Li, H. Jia, F. Seidi, X. Shi, R. Gu, Y. Guo, Y. Liu, Y. Zhu, F. Wu, H. Xiao, Expand and sensitize: guanidine-functionalized exopolysaccharide nanoparticles cause bacterial cell expansion and antibiotic sensitization, Adv. Funct. Mater. 33 (2023) 2305977, https://doi.org/10.1002/adfm.202305977.

[56] S. Li, B. Gu, X. Li, S. Tang, L. Zheng, E. Ruiz-Hitzky, Z. Sun, C. Xu, X. Wang, MXene-enhanced chitin composite sponges with antibacterial and hemostatic activity for wound healing, Adv. Healthc. Mater. 11 (2022) 2102367, https://doi.org/10.1002/adhm.202102367.

[57] C. Jin, D. Sun, Z. Sun, S. Rao, Z. Wu, C. Cheng, L. Liu, Q. Liu, J. Yang, Interfacial engineering of Ni-phytate and $Ti_3C_2T_x$ MXene-sensitized TiO2 toward enhanced sterilization efficacy under 808 nm NIR light irradiation, Appli. Catal. B 330 (2023) 122613, https://doi.org/10.1016/j.apcatb.2023.122613.

[58] X. Peng, X. Meng, B. Yu, H. Chen, Z. Liu, M. Tang, Y. Zheng, Y. Sun, W. Lu, Y. Dai, Graphitized and flexible porous textile updated from waste cotton for wearable electromagnetic interference shielding, Carbon 207 (2023) 144–153, https://doi.org/10.1016/j.carbon.2023.02.044.

[59] X. Zheng, W. Nie, Q. Hu, X. Wang, Z. Wang, L. Zou, X. Hong, H. Yang, J. Shen, C. Li, Multifunctio- nal $RGO/Ti_3C_2T_x$ MXene fabrics for electrochemical energy storage, electromagnetic interference shielding, electrothermal and human motion detection, Mater. Des. 200 (2021) 109442, https://doi.org/10.1016/j.matdes.2020.109442.